The Journal of Supercritical Fluids 225 (2025) 106693

Contents lists available at ScienceDirect

The Journal of Supercritical Fluids

journal homepage: www.elsevier.com/locate/supflu

Optimization and performance evaluation of equations of state for supercritical CO_2-rich mixtures for application in the NET Power cycle

Iván Velázquez [a,*], Frederiek Demeyer [b], Miriam Reyes [a]

[a] Department of Energy and Fluid Mechanics Engineering, University of Valladolid, Paseo del Cauce 59, Valladolid 47011, Spain
[b] Department of Mechanics & Thermal Processes, Engie R&I (Laborelec), Rodestraat 125, Linkebeek 1630, Belgium

HIGHLIGHTS

- Equations of state were optimized for application in the novel NET Power cycle.
- LKP EoS captured the CO_2 - H_2O bubble and dew lines with the lowest error, 2.03 %.
- GERG-2008 captured the density of the sCO_2 mixtures with the lowest error, 1.34 %.
- The GERG-2008 specific work was 32.91 kJ kg^{-1}, up to 1.71 lower than other EoSs.

GRAPHICAL ABSTRACT

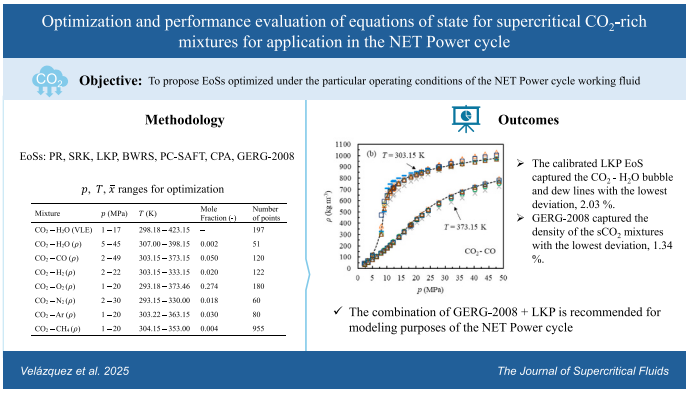

ARTICLE INFO

Keywords:
NET Power cycle
Supercritical carbon dioxide
Equations of state
Interaction parameters

ABSTRACT

In this paper the interaction parameters of six equations of state (EoS) were calibrated from density and phase equilibrium experimental data of supercritical CO_2-rich mixtures. The Peng-Robinson (PR), Soave-Redlich-Kwong (SRK), Lee-Kesler-Plöcker (LKP), Benedict-Webb-Rubin-Starling (BWRS), perturbed chain SAFT (PC-SAFT) and Cubic-Plus-Association (CPA) EoSs were considered. As a novelty, the pressure, temperature and composition ranges for calibration were (1 – 49) MPa, (293.18 – 423.15) K, and (72.6 – 99.8) % mol CO_2, which are close to those found in the innovative oxy-combustion NET Power cycle, particularizing the optimization of the EoSs for application in this power cycle. The performance of the EoSs, including the GERG-2008 EoS, was assessed in an isentropic compression process from 7.4 MPa to 30 MPa. The LKP EoS reported the lowest average deviation, 2.03 %, in modeling the bubble and dew lines of the supercritical CO_2 – H_2O mixture. The GERG-2008 EoS was the most reliable model capturing the density of the supercritical CO_2-rich mixtures, reporting an average deviation of 1.34 %. Therefore, the combination GERG-2008 + LKP is recommended for NET Power cycle modeling purposes. Only the CPA and GERG-2008 models captured the liquid-like properties of the CO_2-rich mixture during the compression. This resulted in a specific compression work of 33.02 kJ kg^{-1} for GERG-2008, while the PR, SRK, LKP, and PC-SAFT EoSs reported a value up to 1.54, 1.65, 1.53, and 1.70 times higher.

* Corresponding author.
E-mail address: ivan.velazquez@uva.es (I. Velázquez).

https://doi.org/10.1016/j.supflu.2025.106693
Received 30 April 2025; Received in revised form 28 May 2025; Accepted 9 June 2025
Available online 11 June 2025

Nomenclature

a	molar Helmholtz free energy, J·mol^{-1}
c_p	specific heat at constant pressure, kJ·kg^{-1}·K^{-1}
h	specific enthalpy, kJ·kg^{-1}
N	number of points
p	pressure, MPa
p_c	critical pressure, MPa
p_r	reduced pressure; (p/p_c)
R	universal gas constant, J·mol^{-1}·K^{-1}
r	pressure ratio
s	specific entropy, kJ·kg^{-1}·K^{-1}
T	temperature, K
T_c	critical temperature, K
T_r	reduced temperature; (T/T_c)
v	specific volume, m^3·kg^{-1}
v_m	molar volume, m^3·mol^{-1}
v_r	reduced volume; $(\frac{p_r}{RT_r\rho})$
w	specific work, kJ·kg^{-1}
x	mole fraction in the liquid phase
$\overline{x}$	molar composition of the mixture
y	mole fraction in the gas phase
z	compressibility factor

Greek letters

Φ	"maximum-likelihood" objective function
α	alpha function
β	volumetric expansivity, K^{-1}
μ	dynamic viscosity, Pa·s
ρ	mass density, kg·m^{-3}
ρ_m	molar density, mol·mL^{-1}
σ	standard deviation
ω	acentric factor

Subscripts

c	critical
cal	calculated
exp	experimental
i, j	Component index
in	inlet
out	outlet

Superscripts

0	simple fluid
assoc	association
disp	dispersion
hc	hard-chain
hs	hard-sphere
R	reference
res	residual

Acronyms

AARD	average of absolute relative deviation, %
BWRS	Benedict-Webb-Rubin-Starling
CPA	Cubic-Plus-Association
EOS-CG	equation of state of combustion gases
LKP	Lee-Kesler-Plöcker
PC-SAFT	perturbed chain – statistical associating fluid theory
PR	Peng-Robinson
RHE	recuperative heat exchanger
SAFT	statistical associating fluid theory
sCO_2	supercritical CO_2
SRK	Soave-Redlich-Kwong
VLE	vapor-liquid equilibrium

1. Introduction

The NET Power cycle uses an oxy-combustion process of natural gas and oxygen to produce emission-free energy with high efficiency, ~ 55.8 % [1], capturing essentially 100 % of the CO_2 emissions [2]. Fig. 1 shows a process flow diagram of the most up-to-date NET Power cycle embodiment [3]. In the oxy-combustor, natural gas (fuel) is introduced with an oxidizing stream (OX-3) to carry out the combustion process at near stoichiometric conditions [4]. The pressurized sCO_2-rich recirculating stream RE-7 moderates the combustion temperature. The resulting CO_2-rich flue gases (FG-1), at 30 MPa and 1423.15 K, are expanded to 3.4 MPa to produce electrical energy. Then, the gases (FG-2) are cooled below the dew point in a recuperative heat exchanger (RHE) to preheat the recirculating TC-1, RE-6 and OX-2 streams [3,5]. After condensation and water removal (FG-4), the CO_2 produced in the combustion is captured and the remainder (RE-1) is compressed up to 8 MPa [1]. The fluid is further cooled to the supercritical liquid-like phase (RE-2), which is characterized by liquid-like densities ($\rho \sim 10^3$ kg m^{-3}) and gas-like viscosities ($\mu \sim 10^{-5}$ Pa s). The resulting dense gases are further compressed to 30 MPa by the REP-1–2 and OXP pumps before being introduced into the RHE and recirculated back to the combustor.

Compressing the RE and OX mixtures near the critical point is beneficial because the specific volume of the fluid is reduced, resulting in low compression work flows and high cycle efficiencies. Thus, with the aim of conducting reliable performance assessments of the NET Power cycle, accurately modeling the volumetric and phase behavior of the sCO_2-rich working fluid, in particular near the critical point, is essential. However, in the region close to the critical point, strong non-idealities appear in the fluid behavior. A pressure – specific enthalpy (h) diagram for pure CO_2 around the critical point is shown in Fig. 2. Isocontours of the compressibility factor (z), and the product of the volumetric expansivity (β) and temperature, βT, were included. z denotes the deviation of a real gas from the ideal gas behavior, and it is defined as:

$$z = \frac{pv}{RT}. \tag{1}$$

In addition, a general relation for the specific enthalpy change of real gases is written in Eq. (2), with β defined in Eq. (3).

$$dh = c_p dT + v(1 - \beta T)dp, \tag{2}$$

$$\beta = \frac{1}{v}\left(\frac{\partial v}{\partial T}\right)_p, \tag{3}$$

The isotherm lines depicted in Fig. 2 are derived from Eq. (2) as follows:

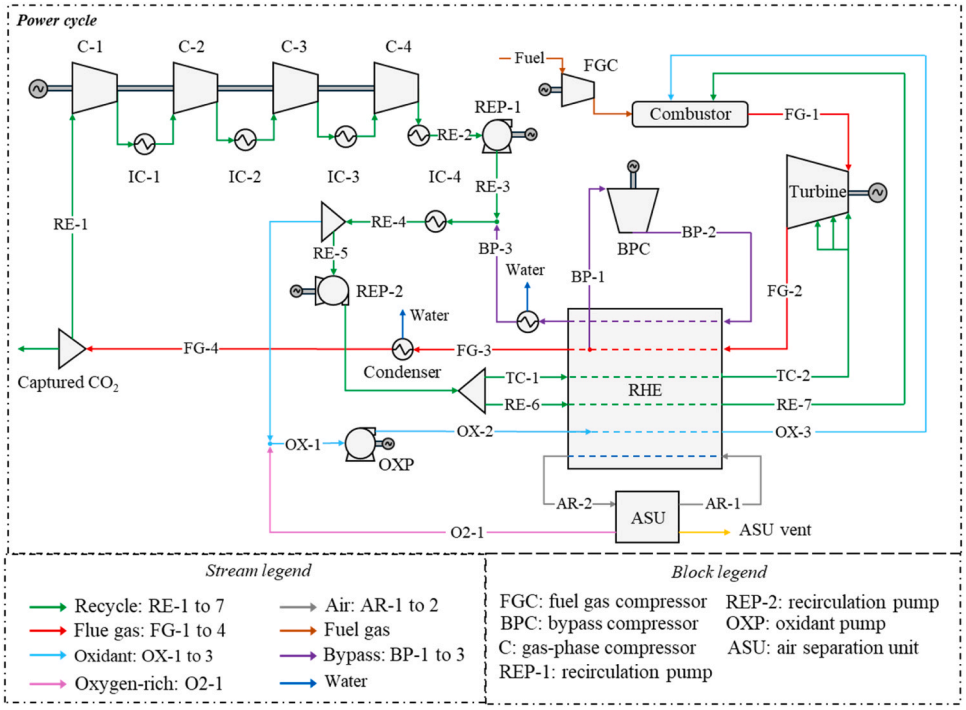

Fig. 1. Process flow diagram of the NET Power cycle.

$$\left(\frac{\partial h}{\partial p}\right)_T = v(1-\beta T). \tag{4}$$

The CO_2 at high temperatures approaches the ideal gas behavior, with values of z close to unity. For ideal gases, $\beta T = 1$, and thus $(\partial h/\partial p)_T = 0$, which implies that the enthalpy is a function of the temperature only, so the isotherm lines become vertical lines. As the critical temperature of CO_2 ($\approx$ 304 K) is approached, the fluid departs from the ideal gas behavior, as noticed by a dramatic change of z. As the CO_2 approaches the critical point, $\beta T > 1$, which means that, according to Eq. (4), there is a deflection of the isotherm lines to lower enthalpy values as the pressure increases. This leads to a sharp change in the enthalpy for a slight change in temperature, as a subcritical phase change, but without phase coexistence. The line formed by connecting the points where $(\partial z/\partial T)_p$ reaches maximum values is called the discontinuity line [6]. In this supercritical phase change, the fluid exhibits strong variations in the thermo-physical properties, which indicates that the discontinuity line separates two regions where the fluid presents liquid-like and gas-like properties. The change of properties is not radical, but occurs in a continuous manner within the discontinuity band. The higher the pressure, the smoother these variations are and occur over a wider temperature range.

In addition to the strong non-idealities, to predict the physical properties of the NET Power cycle working fluid, it should be noted that the impurities present in the sCO_2 streams, H_2O, CO, H_2, O_2, N_2, Ar, CH_4, significantly vary the thermo-physical properties of CO_2 in a non-linear fashion [7,8]. To characterize these sCO_2-rich mixtures, several approaches can be applied: (i) cubic EoSs [9,10]; (ii) theoretical models based on statistical mechanics theories, such as Statistical Associating Fluid Theory (SAFT) and Cubic-Plus-Association (CPA) [11] [12], [8]; and (iii) multiparametric EoSs formulated in terms of the Helmholtz free energy, such as GERG-2008 EoS [13].

Li et al. [14] studied the reliability of the Peng-Robinson (PR),

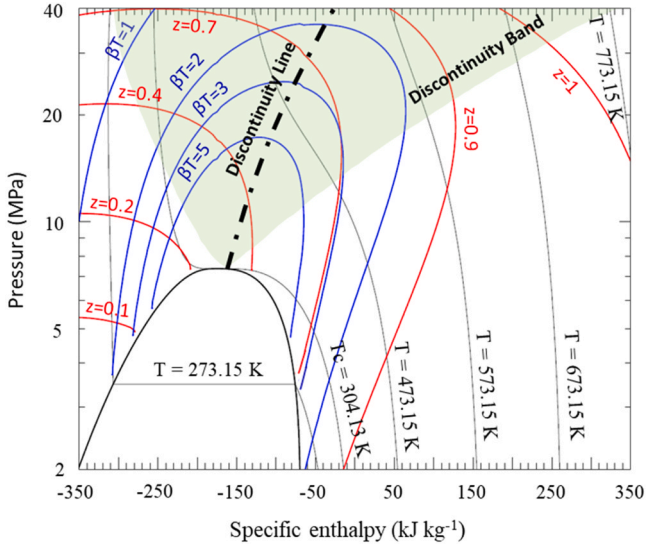

Fig. 2. Pressure – specific enthalpy diagram for pure CO_2 in the region close to the critical point, including constant value lines for temperature, compressibility factor and βT.

Patel-Teja, Redlich-Kwong, Soave-Redlich-Kwong (SRK), modified SRK, modified PR, and improved SRK, in predicting the gas and liquid volumes of supercritical CO_2 binary mixtures, containing CH_4, H_2S, SO_2, Ar and N_2, for temperature and pressure ranges of 89 – 511 K and 0.1 – 69 MPa. The authors concluded that the PR and the Patel-Teja EoSs are generally superior to the rest of EoSs. Xiong et al. [15] presented a novel general cross-association explicit formulation for different bonding types with the aim of increasing the computational efficiency of the CPA

EoS. The new formulation resulted in a CPU time decrease of 70 %. Mazzoccoli et al. [16] selected for comparison the Advanced PR, CPA and GERG-2008 EoSs. Density data for 27 CO_2 mixtures and Vapor-Liquid Equilibrium (VLE) data for 20 different CO_2 mixtures were collected. GERG-2008 EoS reported more accurate results for density and bubble point. However, the GERG-2008 EoS, which was developed for natural gas mixtures, presents shortcomings concerning the modeling of the phase behavior of CO_2 mixtures, underestimating the solubility of gases in the aqueous phase [17]. The equation of state of combustion gases (EOS-CG), developed by Gernert et al. [17], addresses the deficiencies of the GERG-2008 EoS, proposing new adapted departure functions while maintaining the mathematical formulation of the GERG-2008 EoS. The authors compared the performance of the EOS-CG with the GERG-2008, based on experimental data of binary and multicomponent mixtures with high CO_2 content, including H_2O, N_2, O_2, Ar, and CO. The results indicated a clear superiority of the EOS-CG. The EOS-CG model was recently updated and extended into a new model EOS-CG-2021 [18]. Ke et al. [19] experimentally measured the density of the CO_2 – Ar – N_2 ternary mixture (with a mole fraction of Ar and N_2 of 0.05) in a temperature range between 293.15 – 333.15 K, up to a pressure of 23 MPa. Then, authors conducted a comparative study of the GERG-2008, EOS-CG, gSAFT and PR EoSs. The EOS-CG gave the lowest relative deviation for both phase equilibrium and density. McKay et al. [20] analyzed the capability of the PR, SRK, PC-SAFT, GERG-2008 and EOS-CG models to characterize CO_2-rich mixtures. Results revealed relative errors of the PR and SRK EoSs predicting the CO_2 solubility in H_2O of 88.6 % and 89.9 %, respectively. GERG-2008 and EOS-CG reported an error of less than 1 % computing the density of multicomponent CO_2-rich systems over a temperature and pressure range of 273.15 – 423.15 K and 1.1 – 126 MPa. PR and SRK EoSs, with the Peneloux volume shift, reported deviations of 2.8 % and 4.8 % within the supercritical phase. SAFT models demonstrated similar performance to the cubic EoSs.

The performance of the EoSs under the specific operating conditions of the NET Power cycle has not been previously evaluated. Therefore, in this paper the interaction parameters of the PR, SRK, Lee-Kesler-Plöcker (LKP), BWRS, PC-SAFT and CPA EoSs were calibrated based on experimental density and VLE data of sCO_2-rich mixtures collected from the literature. As a novelty, the p, T, $\bar{x}$ optimization conditions were chosen to be close to those found in the NET Power cycle. The performance of the calibrated EoSs, and the GERG-2008 EoS, was then compared, and their influence on a compression process was evaluated. The methodology for performing the EoSs calibration and the compression modeling approach are discussed in Section 2. Then, results are discussed in Section 3. Finally, Section 4 presents the main conclusions and findings of this study.

2. Methodology and assumptions

The methodology for the calibration of the interaction parameters of the EoSs is presented in Section 2.1. Then, Section 2.2 describes the modeling approach of the compression process for supercritical sCO_2-rich mixtures, which is used to evaluate the influence of the EoSs.

2.1. Optimization of the interaction parameters of the equations of state

2.1.1. Selected equations of state: mathematical formulation and mixing rules

Six EoSs were selected as candidates to accurately predict the volumetric behavior of sCO_2 mixtures within the NET Power cycle:

- Peng-Robinson (PR) and Soave-Redlich-Kwong (SRK) cubic-type EoSs.
- Lee-Kesler-Plöcker (LKP) and Benedict-Webb-Rubin-Starling (BWRS) virial-type EoSs.
- Perturbed Chain – Statistical Associating Fluid Theory (PC-SAFT) and Cubic-Plus-Association (CPA) SAFT-type EoSs.

The mathematical formulation, parameters and mixing rules of these EoSs are given in Table 1. The binary interaction parameters that are calibrated in this work were highlighted in bold in Table 1. These EoSs were chosen because: (i) they are the most widely used EoSs for modeling purposes of CO_2 capture and use systems [21], as found after the thorough literature survey; and (ii) they are integrated in the Aspen Plus software. The former is fundamental, since Aspen Plus is the most widely employed process simulation software for conducting thermodynamic studies of the NET Power cycle. Therefore, authors can easily apply the calibrated EoSs proposed in this work for their research. It is worth noting that Aspen Plus contains the formulation of the EoSs presented in Table 1, which ensures that the results presented in this work can be reproduced without the need to use the computational package. In Table 1, x_i represents the mole fraction of component i in the mixture, with the summations running over all components. Pure component parameters, required for the computation of the EoSs, such as critical parameters ($p_{c,i}$, $T_{c,i}$, $\rho_{c,i}$), acentric factors (ω_i), number of spherical segments in a chain (m_i), segment diameters (σ_i), dispersion energies (ε_i/k), number of sites (N_i), and association volume parameters (β_i), for the components CO_2, H_2O, CO, H_2, O_2, N_2, Ar and CH_4, are provided in the Appendix A of the supplementary material. Moreover, specific expressions and constants required by the LKP, BWRS and PC-SAFT EoSs are given in Appendix B, C, and D, respectively. The PC-SAFT EoS is expressed in terms of the molar residual Helmholtz free energy, a^{res}. a is one of the fundamental state functions in thermodynamics. Therefore, all thermodynamic properties can be calculated easily from derivatives of a with respect to the density and temperature. For more details on the derivation of the properties from a see [13]. The performance of these EoSs was compared with the multiparametric GERG-2008 EoS. The detailed mathematical formulation of the GERG-2008 EoS can be found in [13].

2.1.2. Experimental data: pressure, temperature and composition ranges

In the NET Power cycle, the most prominent real gas effects appear in the mixtures RE and OX (see Fig. 1) during the liquid-like compression stages within the discontinuity band. Consequently, the p, T ranges found in such compression, and the composition of the mixtures RE and OX, are the conditions under which the calibration procedure of the EoSs was performed. The mixtures RE and OX are compressed in the REP-1, REP-2 and OXP pumps (see Fig. 1) from 8 MPa to 30 MPa [1]. During the compression, the temperature of the mixtures increases from about 299.15 K to 318.15 K [33], which is close to the critical temperature of CO_2. The molar composition of the RE and OX streams, which were obtained from a NET Power cycle numerical model developed in Aspen Plus, are shown in Table 2.

Experimental density and VLE data for sCO_2-rich binary mixtures were used to perform the calibration of the binary interaction parameters of the EoSs mixing rules. Table 3 presents the p, T, $\bar{x}$ ranges, and the number of experimental data points used during the numerical fitting.

Experimental data were collected over the widest possible pressure

Table 1
Mathematical formulation, parameters, and mixing rules of the selected EoSs. The adjustable binary interaction parameters are highlighted in bold.

EoS	Functional form	Parameters and mixing rules of the EoSs
PR [22]	$p = \frac{RT}{v_m - b} - \frac{a}{v_m(v_m+b)+b(v_m-b)}$	$a = \sum_i\sum_j x_i x_j (1-\boldsymbol{k}_{ij})\sqrt{a_i a_j}$; $b = \sum_i x_i b_i$; $k_{ij} = \boldsymbol{k}_{ij}^{(1)} + \boldsymbol{k}_{ij}^{(2)}T + \frac{\boldsymbol{k}_{ij}^{(3)}}{T}$, $(k_{ij} = k_{ji})$; where a_i and b_i are calculated based on $p_{c,i}$, $T_{c,i}$, ω_i, and the alpha function α_i: $a_i = \alpha_i 0.45724\frac{R^2T_{c,i}^2}{p_{c,i}}$; $b_i = 0.07780\frac{RT_{c,i}}{p_{c,i}}$;$\alpha_i = \left[1+\left(0.37464+1.54226\omega_i-0.26992\omega_i^2\right)\left(1-T_r^{0.5}\right)\right]^2$.
SRK [23]	$p = \frac{RT}{v_m - b} - \frac{a}{v_m(v_m+b)}$	$a = \sum_i\sum_j x_i x_j (1-\boldsymbol{k}_{ij})\sqrt{a_i a_j}$; $b = \sum_i x_i b_i$; $k_{ij} = \boldsymbol{k}_{ij}^{(1)} + \boldsymbol{k}_{ij}^{(2)}T + \frac{\boldsymbol{k}_{ij}^{(3)}}{T}$, $(k_{ij} = k_{ji})$; Where a_i and b_i are calculated based on $p_{c,i}$, $T_{c,i}$, ω_i, and the alpha function α_i: $a_i = \alpha_i 0.42747\frac{R^2T_{c,i}^2}{p_{c,i}}$; $b_i = 0.08664\frac{RT_{c,i}}{p_{c,i}}$;$\alpha_i = \left[1+\left(0.48508+1.55171\omega_i-0.15613\omega_i^2\right)\left(1-T_r^{0.5}\right)\right]^2$.
LKP [24]	$z = z^0 + \frac{\omega}{\omega^R}\left(z^R - z^0\right)$ z^0 and z^R rely on the functional form of the BWR EoS. z^0 is an EoS for simple fluids and z^R is an EoS for a reference fluid (*n*-octane): $z^{(0\text{ or }R)} = 1 + \frac{B}{v_r} + \frac{C}{v_r^2} + \frac{D}{v_r^5} + \frac{c_4\tau^3}{v_r^2} + \left(\beta + \frac{\gamma}{v_r^2}\right)\exp\left(-\frac{\gamma}{v_r^2}\right)$	$B = b_1 - b_2\tau - b_3\tau^2 - b_4\tau^4$; $C = c_1 - c_2\tau + c_3\tau^3$; $D = d_1 + d_2\tau$; where: $v_r = \frac{p_r}{RT_r\rho}$; $\tau = T_r/T$; $\delta = \rho/\rho_r$. The mixing rules are the following: $T_r = \rho_r^{0.25}\sum_i\sum_j x_i x_j v_{c,ij}^{0.25} T_{c,ij}$; $\frac{1}{\rho_r} = \sum_i\sum_j x_i x_j v_{c,ij}$; $p_r = (0.2905 - 0.085\omega)RT_r\rho_r$; with: $T_{c,ij} = \left(1+\boldsymbol{k}_{ij}\right)\left(T_{c,i}\bullet T_{c,j}\right)^{0.5}$, $(k_{ij} = k_{ji})$; $v_{c,ij} = \left(v_{c,i}^{1/3} + v_{c,j}^{1/3}\right)^{3/8}$;$v_{c,i} = (0.2905 - 0.085\omega_i)\frac{RT_{c,i}}{p_{c,i}}$; $\omega = \sum_i x_i\omega_i$;Constants b_1, b_2, b_3, b_4, c_1, c_2, c_3, c_4, d_1, d_2, β and γ are given in Table B.1 (Appendix B) [25].
BWRS [26]	$p = \rho_m RT + \left(B_0RT - A_0 - \frac{C_0}{T^2} + \frac{D_0}{T^3} - \frac{E_0}{T^4}\right)\rho_m^2 + \left(bRT - a - \frac{d}{T}\right)\rho_m^3 + \alpha\left(a + \frac{d}{T}\right)\rho_m^6 + \frac{c\rho_m^3}{T^2}(1+\gamma\rho_m^2)\exp(-\gamma\rho_m^2)$	$B_0 = \sum_i x_i B_{0,i}$; $A_0 = \sum_i\sum_j x_i x_j A_{0,i}^{\frac{1}{2}} A_{0,j}^{\frac{1}{2}}\left(1-\boldsymbol{k}_{ij}\right)$; $C_0 = \sum_i\sum_j x_i x_j C_{0,i}^{\frac{1}{2}} C_{0,j}^{\frac{1}{2}}\left(1-\boldsymbol{k}_{ij}\right)^3$; $D_0 = \sum_i\sum_j x_i x_j D_{0,i}^{\frac{1}{2}} D_{0,j}^{\frac{1}{2}}\left(1-\boldsymbol{k}_{ij}\right)^4$; $E_0 = \sum_i\sum_j x_i x_j E_{0,i}^{\frac{1}{2}} E_{0,j}^{\frac{1}{2}}\left(1-\boldsymbol{k}_{ij}\right)^5$, $(k_{ij} = k_{ji})$; where: $a = \left[\sum_i x_i\alpha_i^{\frac{1}{3}}\right]^3$; $b = \left[\sum_i x_i b_i^{\frac{1}{3}}\right]^3$; $c = \left[\sum_i x_i c_i^{\frac{1}{3}}\right]^3$; $d = \left[\sum_i x_i d_i^{\frac{1}{3}}\right]^3$; $\alpha = \left[\sum_i x_i\alpha_i^{\frac{1}{3}}\right]^3$; $\gamma = \left[\sum_i x_i\gamma_i^{\frac{1}{2}}\right]^2$; Parameters $A_{0,i}$, $B_{0,i}$, $C_{0,i}$, $D_{0,i}$, $E_{0,i}$, a_i, b_i, c_i, d_i, α_i and γ_i for component i are calculated by using Eqs. (C.1) – (C.11), with A_j and B_j listed in Table C.1 (Appendix C) [27].
PC-SAFT [28]	$\frac{a^{res}}{RT} = \frac{a^{hc}}{RT} + \frac{a^{disp}}{RT} + \frac{a^{assoc}}{RT} + \frac{a^{polar}}{RT}$	$a^{hc}/(RT) = \overline{m}\frac{a^{hs}}{RT} - \sum_i x_i(m_i-1)\ln g_{ij}^{hs}$, is the hard-chain term. $a^{disp}/(RT) = -2\pi\rho_m I_1 X - \pi\rho_m\overline{m}C_1 I_2 Y$, is the dispersion term. $a^{assoc}/(RT) = \sum_i x_i\sum_A N_i\left(\ln X^{A_i} - \frac{X^{A_i}}{2} + \frac{1}{2}\right)$, is the association term. $a^{polar}/(RT) = \frac{[a_2/(RT)]}{1-[a_3/(RT)]/[a_2/(RT)]}$, is the polar term. All the details for the calculation of the contribution terms and the formulation of the adjustable interaction parameters $\boldsymbol{k}_{ij}$ are provided in the Appendix D [28–30].
CPA [31], [11]	$p = \frac{RT}{v_m - b} - \frac{a}{v_m(v_m+b)} - 0.5\frac{RT}{v_m}\left(1+\rho_m\frac{\partial \ln g}{\partial\rho_m}\right)\sum_i x_i\sum_{A_i}\left(1-X^{A_i}\right)$. The cubic (physical) term is calculated by the SRK EoS.	$a = \sum_i\sum_j x_i x_j (1-\boldsymbol{k}_{ij})\sqrt{a_i a_j}$; $b = \sum_i x_i b_i$; $k_{ij} = \boldsymbol{k}_{ij}^{(1)} + \boldsymbol{k}_{ij}^{(2)}\frac{T}{T_{ref}}$, $T_{ref} = 298.15$ K, $(k_{ij} = k_{ji})$; $a_i = \alpha_i 0.42748\frac{R^2T_{c,i}^2}{p_{c,i}}$; $b_i = 0.08664\frac{RT_{c,i}}{p_{c,i}}$;$\alpha_i = \left[1+\left(0.48+1.574\omega_i-0.176\omega_i^2\right)\left(1-T_r^{0.5}\right)\right]^2$.$g = (1-1.9\eta)^{-1}$, where $\eta = (b\rho_m)/4$; $X^{A_i} = \left(1+\rho_m\sum_j x_j\sum_B X^{B_j}\Delta^{A_iB_j}\right)^{-1}$; $\Delta^{A_iB_j} = g\beta^{A_iB_j}b_{ij}\left[\exp\left(\frac{\varepsilon^{A_iB_j}}{RT}\right)-1\right]$, with $b_{ij} = (b_i+b_j)/2$. b_i are defined as for the cubic term. Parameters β_i are given in Table A.1 (Appendix A) [32].

Table 2
Composition of the sCO_2-rich mixtures RE and OX.

Component	Mixture RE (% mol)	Mixture OX (% mol)
CO_2	97.9336	75.4445
H_2O	0.1195	0.0920
CO	0.0002	0.0001
H_2	0.0000	0.0000
O_2	0.1963	23.0000
N_2	1.1827	0.9571
Ar	0.5678	0.5063
CH_4	0.0000	0.0000

range, covering the supercritical operating regime, 8 – 30 MPa, where the major real gas effects occur in the NET Power cycle. The temperature range was chosen close to the critical temperature of CO_2. For the CO_2 – O_2 system, the density regression was performed for an O_2 mole fraction of 0.274, which corresponds, approximately, with the typical composition of the mixture OX of the NET Power cycle, as can be found in Table 2. For the remaining mixtures, small values of the impurity mole fraction were selected from the literature, with the aim of mimicking the composition of the mixture RE provided in Table 2.

2.1.3. Equations of state numerical fitting and performance assessment procedures

The softwares Aspen Plus V12.1 [58] and Matlab R2022b [59] were used to calibrate and evaluate the binary interaction parameters of the EoSs of Table 1, from the density and VLE experimental data of sCO_2-rich binary mixtures collected from the literature (Table 3). To this end, a communication between Matlab and Aspen Plus was established through an ActiveX server. A schematic diagram of the numerical procedure for calibration is presented in Fig. 3 [60].

In the first iteration ($l = 0$) a vector $\boldsymbol{k}_{ij}^{l}$, containing the interaction parameters of the EoS, is first initialized to 1 in Matlab. The experimental data of the binary mixture are stored in the Matlab code as vectors of pressure ($\boldsymbol{p}$), temperature ($\boldsymbol{T}$), molar composition ($\overline{\boldsymbol{x}}$), density ($\boldsymbol{\rho}$), equilibrium composition (**VLE**), and standard deviation ($\boldsymbol{\sigma}$). The $\boldsymbol{p}$, $\boldsymbol{T}$, $\overline{\boldsymbol{x}}$ vectors, together with $\boldsymbol{k}_{ij}^{l}$, are sent to Aspen Plus, which contains the formulation of the EoSs shown in Table 1, and calculates the density and equilibrium composition vectors. With the experimental and calculated data, Matlab executes the maximum-likelihood objective function [61], defined in Eq. (5), which is minimized by the optimization algorithm. In Eq. (5), the definition of the maximum-likelihood function is given for either density or VLE regression cases, with N denoting the number of experimental data points. The regression convergence tolerance was set

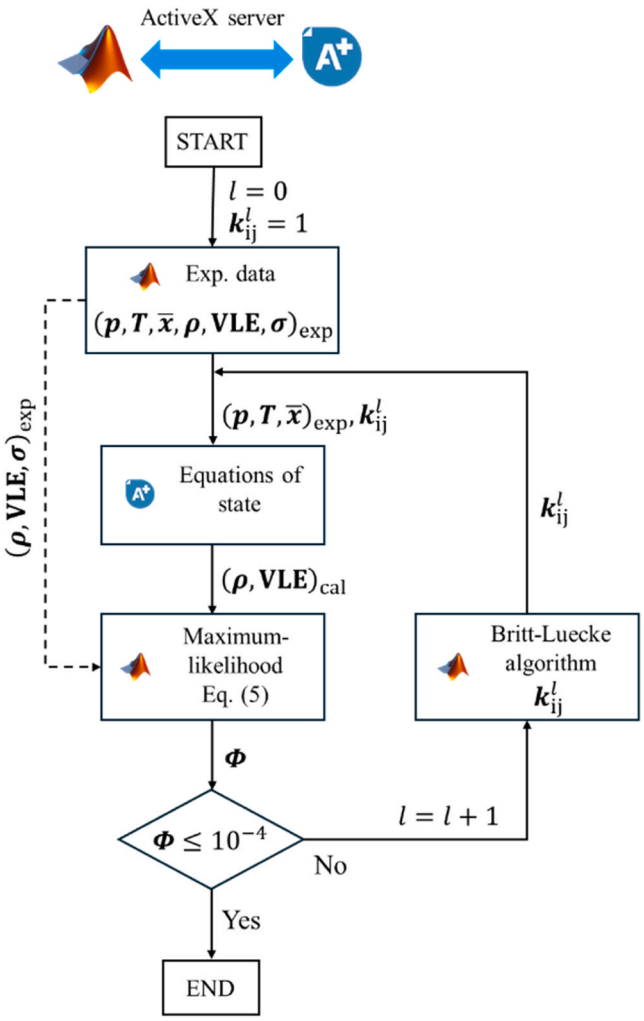

Fig. 3. Flow diagram of the numerical procedure for calibration of the interaction parameters of the EoSs presented in Table 1.

to 10^{-4}. Therefore, when the convergence criterion is satisfied, the optimization procedure is finished. Otherwise, the Britt-Luecke's generalized Least-Square method based optimization algorithm generates an updated set of interaction parameters. For further details about the algorithm refer to [62]. The experimental data and the updated

Table 3
p, T, $\overline{x}$ ranges and number of points of the density and VLE experimental data used for the EoSs numerical calibration.

Mixture	p (MPa)	T (K)	Mole fraction of the impurity	Number of points	References
CO_2 – H_2O (VLE)	1 – 17	298.15 – 423.15	–	197	[34–38]
CO_2 – H_2O (ρ)	5 – 45	307.00 – 398.15	0.002	51	[39–44]
CO_2 – CO (ρ)	2 – 49	303.15 – 373.15	0.050	120	[45]
CO_2 – H_2 (ρ)	2 – 22	303.15 – 333.15	0.020	122	[46,47]
CO_2 – O_2 (ρ)	1 – 20	293.18 – 373.46	0.274	180	[48]
CO_2 – N_2 (ρ)	2 – 30	293.15 – 330.00	0.018	60	[49–55]
CO_2 – Ar (ρ)	1 – 20	303.22 – 363.15	0.030	80	[55]
CO_2 – CH_4 (ρ)	1 – 20	304.15 – 353.00	0.004	955	[56,57]

interaction parameters are sent to Aspen Plus and the optimization procedure is repeated until the convergence tolerance is achieved.

$$\Phi = \begin{cases} \dfrac{1}{N}\sum_{i=1}^{N}\left(\dfrac{\rho_{cal,i}-\rho_{exp,i}}{\sigma_{\rho,i}}\right)^2, \text{ for } \rho \text{ regression;} \\ \dfrac{1}{N}\sum_{i=1}^{N}\left[\left(\dfrac{x_{CO_2,cal,i}-x_{CO_2,exp,i}}{\sigma_{x_{CO_2,i}}}\right)^2+\left(\dfrac{y_{CO_2,cal,i}-y_{CO_2,exp,i}}{\sigma_{y_{CO_2,i}}}\right)^2\right], \text{ for VLE regression.} \end{cases} \quad (5)$$

Once the calibrated interaction coefficients were obtained, they are introduced into the formulation of the EoSs. A quantitative comparison between the results provided by the EoSs and the experimental data was performed to determine the EoS that captures most reliably the experimental data. To carry out this comparison, in the *Simulation* section of Aspen Plus, a material stream was created whose temperature, pressure and composition were established under the same conditions as the experimental data from a code implemented in Matlab. This code contains all the experimental source data and triggers the Aspen model to share the material stream results under the same operational conditions as the source data. As a result, the density and VLE compositions response can be compared between the different EoSs as the deviation towards the source data. To quantify the deviations between the EoSs predictions and the data, the AARD, whose definition is presented in Eq. (6) for density and VLE in the liquid and gas phases cases, was used.

$$\text{AARD (\%)} = \begin{cases} \dfrac{100}{N}\sum_{i=1}^{N}\dfrac{|\rho_{cal,i}-\rho_{exp,i}|}{\rho_{exp,i}}, \text{ for } \rho; \\ \dfrac{100}{N}\sum_{i=1}^{N}\dfrac{|x_{CO_2,cal,i}-x_{CO_2,exp,i}|}{x_{CO_2,exp,i}}, \text{ for VLE in the liquid phase;} \\ \dfrac{100}{N}\sum_{i=1}^{N}\dfrac{|y_{CO_2,cal,i}-y_{CO_2,exp,i}|}{y_{CO_2,exp,i}}, \text{ for VLE in the gas phase.} \end{cases} \quad (6)$$

2.2. Supercritical CO_2-rich mixtures isentropic compression modeling approach

To model the isentropic compression of an ideal gas, it is necessary to establish a relation for the evolution of the gas temperature with the pressure by using Eq. (7).

$$\left(\frac{\partial T}{\partial p}\right)_s = \frac{RT}{pc_p}. \quad (7)$$

Therefore, knowing the temperature change with Eq. (7), and given a pressure ratio, r, the total specific work of compression can be calculated from the change in specific enthalpies by using Eq. (8).

$$w = h(rp_{in}, T_{out}) - h(p_{in}, T_{in}) \quad (8)$$

However, Eq. (7) is not suitable for supercritical fluids; which experience strong real gas effects, especially near the critical point. Hence, an expression relating the evolution of the temperature with the pressure at constant entropy, similar to Eq. (7), but appropriate for real gases, has to be obtained. To this end, the following Maxwell's equation is employed:

$$\left(\frac{\partial T}{\partial p}\right)_s = \left(\frac{\partial v}{\partial s}\right)_p. \quad (9)$$

Considering also the following relation:

$$\left(\frac{\partial v}{\partial s}\right)_p\left(\frac{\partial s}{\partial T}\right)_p\left(\frac{\partial T}{\partial v}\right)_p = 1, \quad (10)$$

Table 5
AARD (%) of the EoSs in the prediction of the VLE composition of CO_2 – H_2O mixtures within the p, T, $\bar{x}$ ranges shown in Table 3.

EoS	Bubble line	Dew line	*Average*
PR	3.83	1.92	2.88
SRK	4.30	1.78	3.04
LKP	2.23	1.83	2.03
BWRS	11.94	1.53	6.74
PC-SAFT	4.95	1.41	3.18
CPA	5.34	1.43	3.39
GERG−2008	8.51	0.25	4.38
Average	15.56	1.45	

Table 4
Calibrated interaction parameters of the PR, SRK, LKP, BWRS, PC-SAFT and CPA EoSs. These interaction parameters correspond to those highlighted in bold in the formulation of the EoSs given in Table 1.

		CO_2 – H_2O		CO_2 – CO	CO_2 – H_2	CO_2 – O_2	CO_2 – N_2	CO_2 – Ar	CO_2 – CH_4
		VLE	ρ	ρ	ρ	ρ	ρ	ρ	ρ
PR	$k_{ij}^{(1)}$	−0.4274	−0.0823492	0.0000	0.0000	−0.144269	0.0000	−0.128005	−0.229886
	$k_{ij}^{(2)}$	0.001	0.00130716	−0.00085152	−0.002656	0.00094759	−0.00109974	0.0000	−0.00093592
SRK	$k_{ij}^{(1)}$	−0.4614	0.0000	0.0000	0.0000	0.0603179	0.0000	−0.189057	0.0000
	$k_{ij}^{(2)}$	0.0011	−0.0010648	0.00149822	−0.021956	0.0000	−0.00087398	0.0000	−0.0789253
LKP	k_{ij}	0.0125	−0.278075	0.114011	0.916455	0.0253371	0.0901669	0.0200776	−0.489781
BWRS	k_{ij}	0.1053	0.0000	−0.181284	−0.681987	0.0130965	−0.476755	−0.033787	0.0531
PC-SAFT	$k_{ij}^{(1)}$	0.1565	0.0929834	−0.999539	−0.284113	0.205097	−0.96324	0.0000	0.0000
	$k_{ij}^{(2)}$	0.1449	0.116352	0.959316	−0.999873	−0.256288	0.996573	0.0732153	0.99997
	$k_{ij}^{(5)}$	0.0228	−0.0494549	−0.0147781	0.0000	0.0000	−0.576246	0.0000	0.998752
CPA	$k_{ij}^{(1)}$	0.168	0.285987	−0.211483	0.0000	0.503948	0.567561	0.0000	−0.412014
	$k_{ij}^{(2)}$	0.269	0.241135	−0.207193	0.0000	−0.455381	−0.011355	−0.037751	0.0000

the following expression is obtained:

$$\left(\frac{\partial T}{\partial p}\right)_s = \left(\frac{\partial v}{\partial T}\right)_p \Big/ \left(\frac{\partial s}{\partial T}\right)_p \tag{11}$$

The derivative of the numerator of the right hand side expression in Eq. (11) can be expressed as a function of β from Eq. (3) as βv. The derivative of the denominator is equivalent to c_p/T [63]. Thus, Eq. (11) can be written as follows:

$$\left(\frac{\partial T}{\partial p}\right)_s = \frac{zRT(\beta T)}{pc_p}. \tag{12}$$

In Eq. (12) a generic real gas EoS relation of the form $pv = zRT$ was replaced. Eq. (12) represents the isentropic evolution of the temperature as a function of the pressure for a real gas mixture. For an ideal gas, βT and z are equal to one, therefore, Eq. (12) becomes Eq. (7) in this case. Finally, the total specific work of compression is computed using the Eq. (8).

The compression model was implemented and solved in Matlab. The differential equation that models the local evolution of the gas temperature with the pressure, Eq. (12), was discretized by using the Euler's method. The model was discretized in 100 steps from the fluid inlet pressure, 7.4 MPa, to the discharge pressure, 30 MPa. The thermodynamic and transport coefficients of the model are calculated by Aspen Plus, where the calibrated EoSs are implemented. Matlab sends, through an ActiveX server, two intensive properties and the mixture composition to Aspen Plus. Then, Aspen Plus calculates the desired properties and sends them back to Matlab. β is not available as an output parameter in Aspen Plus. Thus, β was obtained from Eq. (3), and the derivative was calculated by finite differences.

3. Results and discussion

The results of the numerical calibration and the performance assessment of the EoSs are provided in Section 3.1. Then, the influence of the EoSs on the isentropic compression process, under the operating conditions of the NET Power cycle, is discussed in Section 3.2.

3.1. Results of the numerical calibration of the equations of state

The adjustable binary interaction parameters of the selected EoSs (highlighted in bold in the Table 1), that resulted from the numerical calibration process, are presented in Table 4.

The comparison between the composition of the equilibrium phases of the CO_2 – H_2O mixture calculated by the calibrated EoSs and the experimental VLE data is represented in Fig. E.1 (Appendix E) of the supplementary material. The EoSs predict the solubility of CO_2 in the H_2O-rich liquid phase with a deviation of less than 10 %. All the EoSs predict the composition of the CO_2-rich gas phase within a deviation of 2 % over the entire calibration range. Table 5 shows the AARD in the prediction of the bubble line and dew line by the EoSs with respect to the experimental data. The bubble point prediction, as a function of pressure, by the EoSs presents a larger deviation from the experimental points than the dew point prediction. The average AARD of the EoSs in the bubble line estimation is 15.56 %, while it is 1.45 % for the dew line. The calibrated LKP EoS reports the lowest AARD in the bubble line modeling, 2.03 %, while the BWRS EoS gives the highest AARD, 11.94 %. Concerning the dew line prediction, the GERG-2008 EoS presents the lowest AARD, 0.25 %. The EoS with the lowest average AARD in the prediction of both bubble and dew lines is the LKP, reporting an AARD of 2.03 %. The results also reveal that the cubic PR and SRK EoSs, with an appropriate fitting of the binary interaction parameters, present a lower AARD than other thermodynamic models with more complex mathematical formulation within the pressure and temperature ranges considered in this study [64].

Regarding density predictions, Fig. E.2 (Appendix E) of the supplementary material compares the prediction of the density of sCO_2-rich binary mixtures by the EoSs with respect to the experimental data points. Except for the CO_2 – H_2O and CO_2 – CH_4 mixtures, the EoSs predict the volumetric behavior of the binary mixtures with a deviation of less than 10 % over the entire calibration range. For the CO_2 – CH_4 mixture, all EoSs show significant deviations, up to 126.4 % for CPA, within the discontinuity band. This indicates that the experimental source data of the CO_2 – CH_4 mixture may have a larger uncertainty than expected. Table 6 reports the AARD in the prediction of the density of sCO_2-rich binary mixtures by the EoSs with respect to the experimental data. The volumetric behavior of the CO_2 – H_2O mixture is predicted by the EoSs with an AARD of about two times higher than for the rest of the binary mixtures. This is because the CO_2 – H_2O mixture is highly non-ideal due to the different polarity of the CO_2 and H_2O molecules [8, 65]. The fact that the BWRS EoS is uncapable of accurately predicting the density of the CO_2 – H_2O mixture was the reason for the retirement of its AARD results for this mixture. The results also pointed out that the GERG-2008 is the model that, on average, matches the experimental data with the lowest deviation, presenting an average AARD for all considered mixtures of 1.34 %. Therefore, it is recommended to use the combination of GERG-2008 + LKP for modeling purposes of the NET Power cycle. GERG-2008 is used for volumetric calculations and the calibrated LKP EoS for predicting the phase behavior of the CO_2 – H_2O mixture.

3.1.1. Vapor-liquid equilibrium modeling trends

A pressure-composition diagram for the CO_2 – H_2O mixture, for a temperature of 298.15 K, is shown in Fig. 4. Fig. 4(a) presents the solubility of CO_2 in the H_2O-rich liquid phase and Fig. 4(b) the CO_2 mole fraction in the CO_2-rich gas phase. All calibrated EoSs demonstrate an attenuation in their predictive capability as the temperature of the mixture increases.

PR and SRK EoSs tend to underestimate the solubility of CO_2 in the H_2O-rich liquid phase and the amount of water in the CO_2-rich gas phase. Although this deviation is reduced for high pressure. In general, both cubic EoSs were capable of accurate modeling the VLE of the CO_2 – H_2O mixture. The LKP EoS has fewer discrepancies than the other EoSs in comparison to the experimental data. BWRS EoS predicts a higher solubility of CO_2 in the aqueous phase. LKP and BWRS EoSs present a similar pattern than PR and SRK EoSs in modeling the composition of the vapor phase. However, BWRS predicts a lower H_2O mole fraction in the CO_2 gas phase for pressures above 3.5 MPa. PC-SAFT and CPA EoSs

Table 6
AARD (%) in the density prediction of sCO_2-rich binary mixtures in the p, T, $\bar{x}$ ranges shown in Table 3.

EoS	CO_2 – H_2O	CO_2 – CO	CO_2 – H_2	CO_2 – O_2	CO_2 – N_2	CO_2 – Ar	CO_2 –CH_4	*Average*
PR	3.03	2.30	3.10	1.49	3.17	2.16	3.21	2.98
SRK	18.28	5.65	2.72	3.33	3.50	2.82	2.05	5.30
LKP	2.29	0.62	1.02	1.79	1.82	0.65	0.97	1.78
BWRS	-	1.84	3.40	1.66	4.91	2.47	4.10	2.96
PC-SAFT	2.77	2.10	2.93	2.44	2.46	1.70	1.51	2.33
CPA	3.13	2.21	1.89	1.60	3.71	1.98	2.43	2.44
GERG−2008	2.37	1.51	0.58	1.37	1.10	0.94	0.93	1.34
Average	4.89	2.22	2.03	1.88	2.72	1.71	2.02	

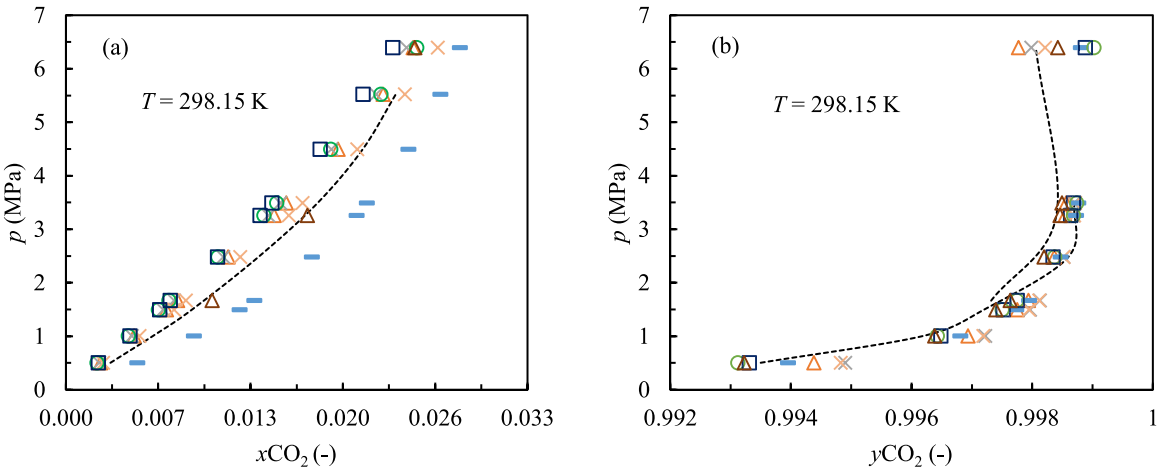

Fig. 4. Pressure-composition phase diagram for the CO_2 – H_2O mixture for a temperature of 298.15 K. (a) H_2O-rich liquid phase and (b) CO_2-rich liquid phase. (-------) Experimental data (△) PR, (⨯) SRK, (⨯) LKP, (▬) BWRS, (○) PC-SAFT, (□) CPA, (△) GERG-2008.

accurately adjust the composition of the phases in equilibrium of the CO_2 – H_2O mixture. However, CPA EoS tends to deviate towards lower values of the gas solubility because of the cubic term contained in its formulation. In addition, PC-SAFT and CPA EoSs underestimate the H_2O fraction dissolved in the CO_2-rich gas phase for high mixture pressures. GERG-2008 shows discrepancies in calculating the solubility of CO_2 in the aqueous phase for pressures below 2 MPa. This deviation is reduced as the mixture pressure increases.

3.1.2. *Density modeling trends*

Fig. 5 represents the evolution of the density of the binary mixtures (a) CO_2 – H_2O, (b) CO_2 – CO, (c) CO_2 – H_2, (d) CO_2 – O_2, (e) CO_2 – N_2, (f) CO_2 – Ar and (g) CO_2 – CH_4, estimated by the calibrated EoSs, compared to the density experimental data, as a function of the pressure and temperature of the mixture. The density gradient becomes steeper as the mixture temperature decreases due to an increase of the isothermal compressibility factor, which intensifies the real gas effects. As a result, the deviation of the EoSs increases at low temperatures. For pressures far away from the corresponding ones in the discontinuity band, the deviation between the density estimated by the EoSs and the experimental data is reduced.

PR and SRK EoSs underestimate the density of the mixtures: CO_2 – H_2O, in the discontinuity band (as also stated by Ibrahim et al. [66]), although PR overestimated the density at pressures above 25 MPa; CO_2 – CO, in the pressure ranges between 7 – 27 MPa, although PR overestimates it at pressures higher than 25 MPa; CO_2 – H_2, in the liquid-like phase, with the deviation decreasing as the mixture pressure increases; CO_2 – N_2, for pressures above 8 MPa; CO_2 – Ar, in the liquid-like phase; and CO_2 – CH_4, from the critical pressure of the mixture up to 18 MPa. This periodic underestimation of the density by PR and SRK EoSs is relaxed as the mixture temperature augments. Beyond the p, T, $\bar{x}$ calibration ranges, results revealed that the deviation of PR and SRK EoSs, compared to the experimental data, increases more than the rest of EoSs, demonstrating that their performance is highly dependent on the binary interaction parameters [12,67]. LKP EoS is able to predict the density evolution within the discontinuity band close to the experimental data, without significant deviations. BWRS EoS yield erroneous densities for the CO_2 – H_2O mixture. However, the rest of the binary mixtures are accurately predicted, tending to overestimate the density of the CO_2 – N_2, CO_2 – Ar and CO_2 – CH_4 mixtures within the liquid-like phase region. PC-SAFT EoS underestimates the density of the CO_2 – O_2 mixture for pressures above 12 MPa. The rest of the EoSs model the density of the CO_2 – O_2 mixture accurately since the O_2 mole fraction used in the numerical regression is high, tending to move the mixture away from the critical point. CPA EoS tends to underestimate the density of the CO_2 – O_2, CO_2 – N_2 and CO_2 – Ar mixtures, although with less deviation than PR and SRK. This is because the physical term of the CPA EoS is precisely the SRK EoS [11]. GERG-2008 accurately matches the experimental data. The deviation of the EoSs decreases as the pressure and temperature increase, especially the former. This is because the deflection of the isotherm lines decreases as the mixture moves away from the critical point.

3.2. *Isentropic compression process*

The isentropic compression process modeled in this study was calculated assuming initial fluid conditions of 303.15 K and 7.4 MPa. The fluid is compressed up to 30 MPa isentropically. To evaluate the influence of the EoSs on the compression process, the mixtures RE and OX were analyzed. The composition of these mixtures was given in Table 2. The fact that BWRS was not able to accurately predict the volumetric behavior of the CO_2 when containing traces of H_2O, as explained in Section 3.1.2, lead to inconsistent results in the evolution of the fluid during compression. For that reason, results from the BWRS EoSs were not considered in this study.

Fig. 6 shows the evolution of (a) temperature, (b) compressibility factor, (c) heat capacity and (d) specific volume as a function of the pressure during the isentropic compression for the mixture RE. The fluid temperature increment during the compression process is lower for the CPA and GERG-2008 EoSs than for the PR, SRK, LKP and PC-SAFT EoSs. For example, for GERG-2008, the temperature change was 51.6 K, and for PC-SAFT 102.2 K. CPA and GERG-2008 predict a lower compressibility factor over the entire pression range in which compression takes place. This means that the fluid is in a denser and less compressible phase. In addition, only the CPA and GERG-2008 EoSs predicted the supercritical phase transition between the liquid-like phase and the gas-like phase, crossing the discontinuity line. This is deduced from Fig. 6(c), where the steep compressibility factor gradient may be observed. This is also noted in Fig. 6(d), where the CPA and GERG-2008 EoSs predict the sharp variation of the specific heat undergone by the fluid during the supercritical phase transition. This implies that the specific heat predicted by CPA and GERG-2008 is higher than that predicted by the rest of EoSs at the beginning of compression, concretely in the pressure range where the supercritical phase change occurs. A lower value of the fluid

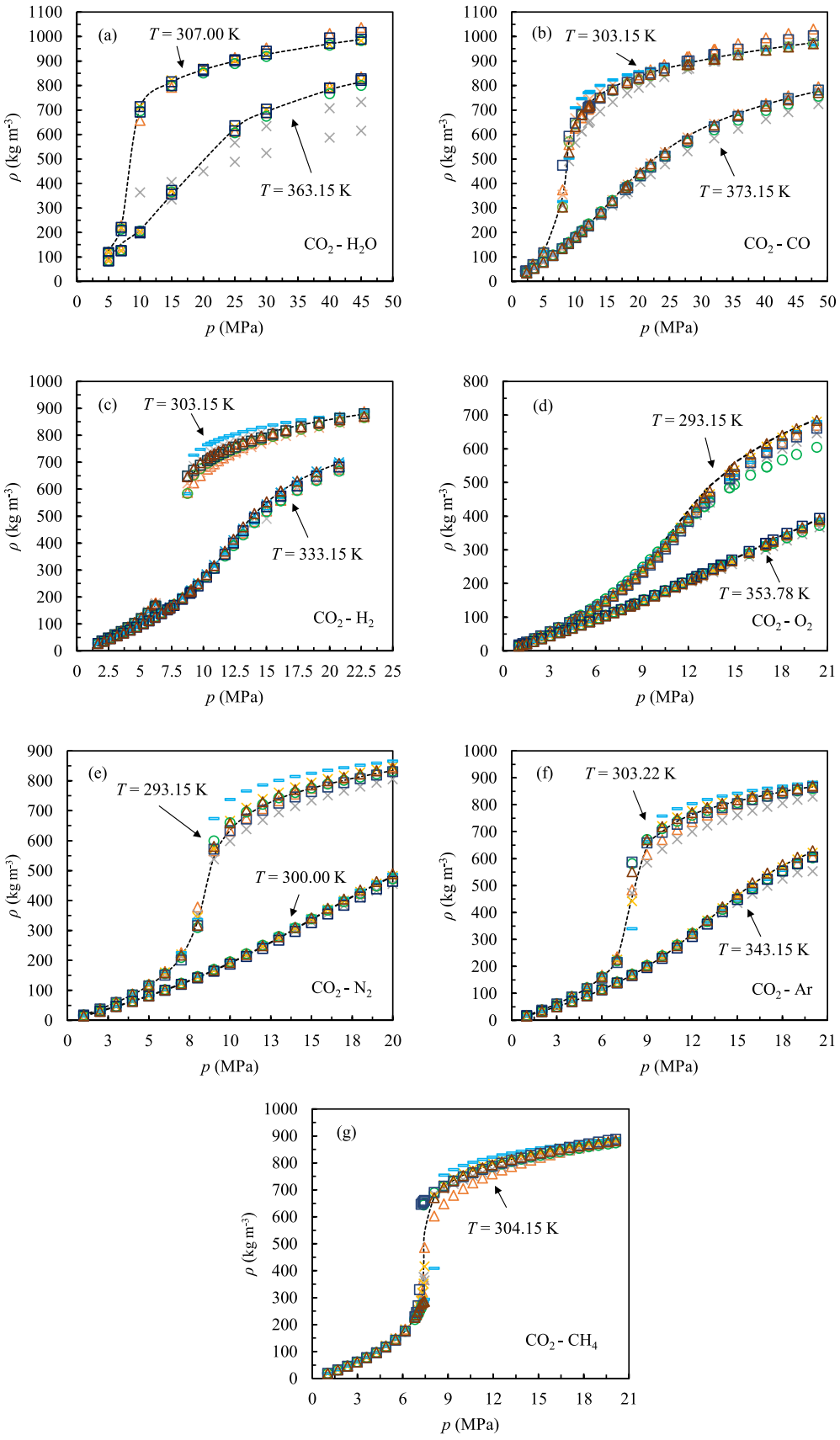

Fig. 5. Evolution of the density as a function of the pressure, for different temperatures, for the binary mixtures: (a) CO_2 – H_2O, (b) CO_2 – CO, (c) CO_2 – H_2, (d) CO_2 – O_2, (e) CO_2 – N_2, (f) CO_2 – Ar, (g) CO_2 – CH_4, calculated by the EoSs and the experimental data used for the interaction coefficient calibration. (-------) Experimental data (△) PR, (×) SRK, (×) LKP, (▬) BWRS, (○) PC-SAFT, (□) CPA, (△) GERG-2008.

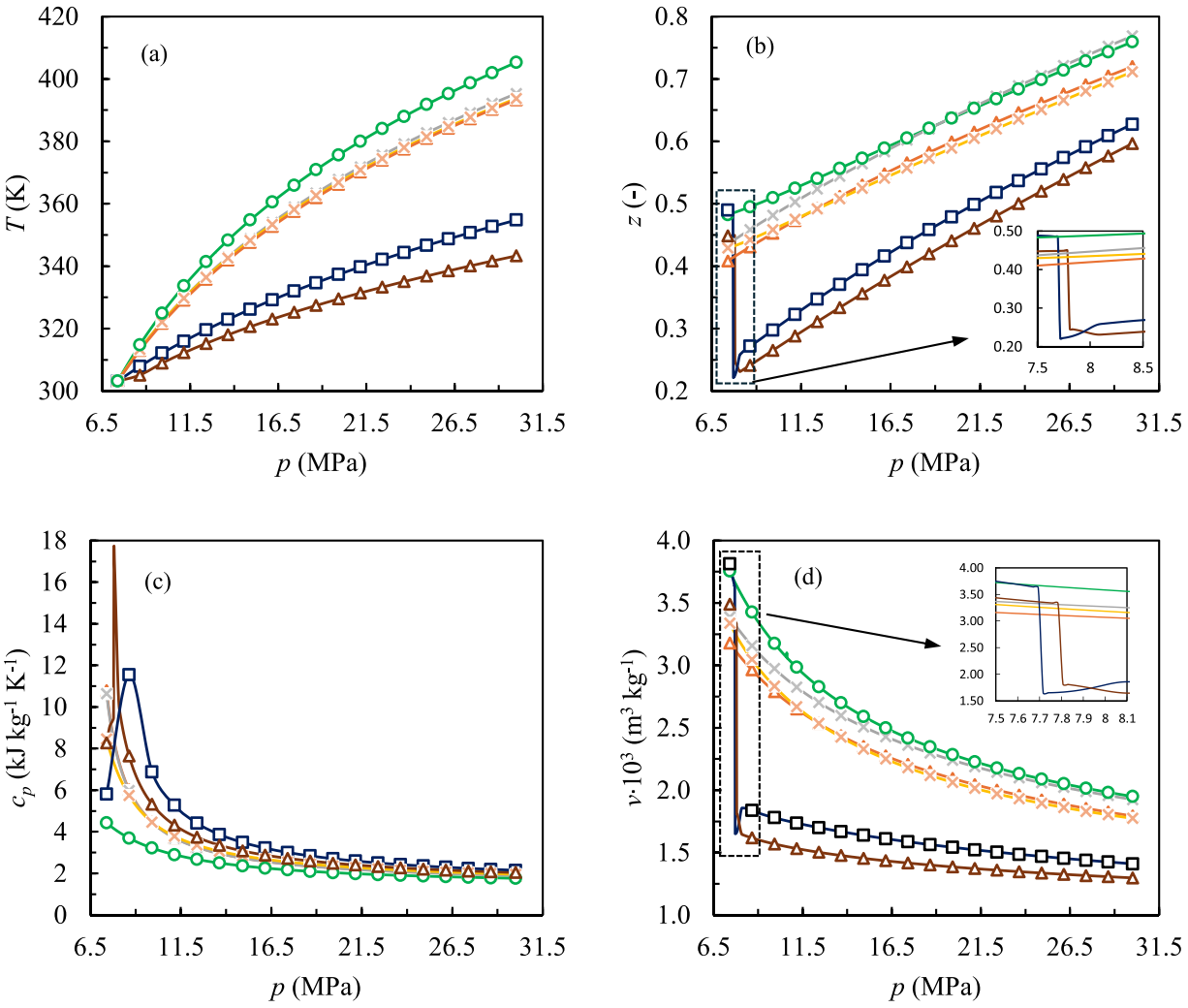

Fig. 6. Evolution of (a) temperature, (b) compressibility factor, (c) specific heat at constant pressure and (d) specific volume, as a function of pressure during the isentropic compression of the mixture RE. (△) PR, (×) SRK, (×) LKP, (○) PC-SAFT, (□) CPA, (△) GERG-2008.

Table 7
Total specific work of compression from 303.15 K, 7.4 MPa to 30 MPa, for the mixture RE, as a function of the EoS.

	PR	SRK	LKP	PC-SAFT	CPA	GERG-2008
w (kJ kg^{-1})	50.82	54.33	50.62	56.19	36.71	33.02
$w/w_{GERG-2008}$ (-)	1.54	1.65	1.53	1.70	1.11	1.00

compressibility factor during compression and a higher value of the specific heat at the beginning of the compression predicted by the CPA and GERG-2008 EoSs result in that, according to Eq. (12), the temperature gradient during compression is lower than that predicted by the rest of the EoSs.

Table 7 presents the total specific work of compression for the mixture RE as a function of the EoS. The temperature and compressibility factor predicted by the CPA and GERG-2008 models over the entire compression range are lower than that computed by the rest of EoSs. This implies that the specific volume of the fluid is lower in the compression and, therefore, the specific work of compression for CPA and GERG-2008 is lower than for the rest of EoSs. Specifically, the specific work of compression computed by the PR, SRK, LKP and PC-SAFT EoSs is more than 1.5 times that for GERG-2008.

This finding reveals that, despite the low deviations in computing the physical properties of the sCO_2 mixtures within the discontinuity band, notable deviations in the prediction of the NET Power cycle compression process are found. Thus, calibration the EoSs for the exact p, T, $\bar{x}$ conditions of the NET Power cycle becomes essential. The compression work flow of the REP-1 and REP-2 pumps accounts for about the 30 % of the total power consumed by the NET Power cycle [3]. If the PR EoS is used instead of the GERG-2008 EoS, the specific compression work of those pumps would be overestimated by a factor of 1.54, as found in Table 7. This would result in an underestimation of the cycle efficiency of about 1.7 %. In addition, the pumps would be oversized, operating beyond the design point, with a consequent reduction of the hydraulic efficiency. Moreover, if the PR EoS is used, the predicted temperature of the RE-6 and TC-1 streams (see Fig. 1) at the recuperator inlet would be higher. This results in a higher temperature of the exhaust gases, FG-3, at the recuperator outlet and, hence, a higher moisture content. Consequently, the predicted heat transfer rates would be lower than actual, leading to an oversized recuperator with higher thermal inertia and cost.

Fig. 7 shows the evolution of the (a) temperature, (b) compressibility factor, (c) specific heat and (d) specific volume as a function of the pressure during the isentropic compression for the mixture OX. The evolution of the temperature and the thermodynamic properties of the

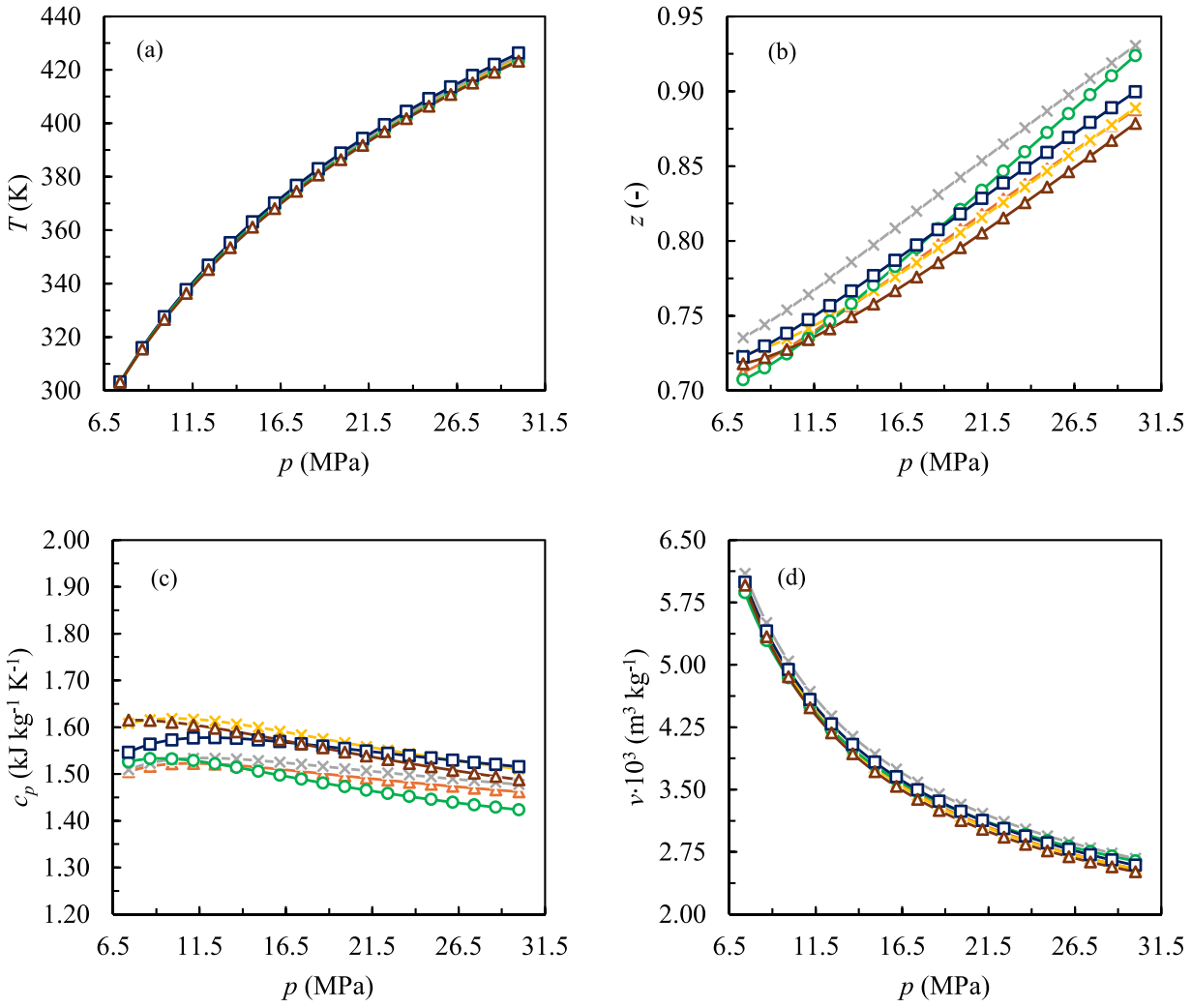

Fig. 7. Evolution of the (a) temperature, (b) compressibility factor, (c) specific heat at constant pressure and (d) specific volume, as a function of pressure during the isentropic compression of the mixture OX. (△) PR, (×) SRK, (×) LKP, (○) PC-SAFT, (□) CPA, (△) GERG-2008.

Table 8
Total specific work of compression from 303.15 K, 7.4 MPa to 30 MPa, for the mixture OX, as a function of the EoS.

	PR	SRK	LKP	PC-SAFT	CPA	GERG-2008
w (kJ kg^{-1})	80.45	83.81	80.52	81.26	81.98	79.33
$w/w_{GERG-2008}$ (-)	1.01	1.06	1.02	1.02	1.03	1.00

fluid during the compression are similar for all EoSs. This is because the compressibility factor is higher than 0.7 during compression, so the real gas effects are less intense than for the RE mixture. The addition of a high amount of O_2 moves the critical point of the mixture with respect to the critical point of pure CO_2. In essence, the critical temperature is reduced, and the critical pressure is augmented. Consequently, a higher compression range takes place when the fluid is in the subcritical superheated gas state, although close to the critical point. The fluid is in the supercritical gas-like region throughout the entire compression range. This justifies the high value of the fluid compressibility factor shown in Fig. 7(b). As the fluid evolves during the compression, the temperature increase causes the fluid to enter deeper into the supercritical gas-like region. Hence, the fluid does not cross the discontinuity line and does not experience the supercritical phase change between the liquid-like and gas-like phase. This is observed in Fig. 7(b-d) by a smooth evolution of the compressibility factor, specific heat and specific volume as a function of the pressure. A high value of the compressibility factor and a low value of the specific heat in compression imply that, according to Eq. (12), the gradient of the temperature rise as a function of pressure is large.

Table 8 presents the total specific compression work for the mixture OX as a function of the EoS. Since the gas temperature during compression increases rapidly due to the high compressibility factor and low specific heat, the specific volume of the mixture is high. As a result, the total specific work of compression obtained by GERG-2008 for the mixture OX is 2.4 times higher than that for the mixture RE. The fact that the real gas effects are not intense for the mixture OX, for the considered compression range, justifies that the total specific work of compression estimated as a function of the EoS is similar.

4. Conclusions

In this paper the interaction parameters of the PR, SRK, LKP, BWRS, PC-SAFT and CPA EoSs were optimized on the basis of experimental density and VLE data of binary sCO_2-rich mixtures collected from the literature. The p, T, $\bar{x}$ ranges for optimization were 1 – 49 MPa, 293.18 –

423.15 K and 72.6 – 99.8 % mol CO_2, which are close to those found in the working fluid of the NET Power cycle. Thus, the EoSs were calibrated for their application under the specific conditions of the NET Power cycle. The accuracy in the volumetric and phase calculations of the aforementioned EoSs, including the GERG-2008 EoS, was evaluated. In addition, the influence of the EoS on a compression process from 7.4 MPa to 30 MPa was studied. Outcomes from this study allows establishing a quantitative criterion for choosing the most reliable EoS for application in numerical thermodynamic studies of the NET Power cycle. The key findings of this research are as follows:

- Regarding the VLE of the CO_2 – H_2O mixture, the EoSs predict the composition of the H_2O-rich liquid phase and the CO_2-rich gas phase within a deviation of 10 % and 2 %, respectively, for a temperature and pressure range of 298.18 – 423.15 K and 1 – 17 MPa. The calibrated LKP EoS reported the lowest average deviation, 2.03 %, computing the bubble and dew lines.
- The calibrated EoSs capture the experimental density of the mixtures CO_2 – CO, CO_2 – H_2, CO_2 – O_2, CO_2 – N_2 and CO_2 – Ar within a deviation of less than 10 %. The volumetric calculation of the mixtures CO_2 – H_2O and CO_2 – CH_4 by the EoSs reported higher inaccuracies. GERG-2008 was the EoS that captured the experimental density data with the highest fidelity, reporting an average AARD of 1.34 %. Therefore, it is recommended to use the combination of GERG-2008 + LKP for thermodynamic modeling purposes of the NET Power cycle. GERG-2008 is used for volumetric calculations, and the calibrated LKP EoS for predicting the phase behavior of the CO_2 – H_2O mixture.
- Cubic EoSs underestimate the density of the supercritical mixtures. It was found that, beyond the calibration p, T, $\bar{x}$ ranges, the deviation reported by the cubic EoSs was larger than the rest of EoSs. In the absence of experimental density data, the theoretical predictive model CPA can be used.
- In the compression process of the mixture sCO_2-rich mixture, only the CPA and GERG-2008 EoSs considered the supercritical phase change and, thus, the liquid-like properties of the mixture during the compression onset. This resulted in a lower compressibility factor and specific volume. The specific compression work calculated by GERG-2008 was 33.02 kJ kg^{-1}, with the PR, SRK, LKP and PC-SAFT EoSs reporting a value of up to 1.54, 1.65, 1.53 and 1.70 times higher, respectively. This finding suggests that an unsuitable choice of the EoS could: (i) underestimate the cycle efficiency by 1.7 %; (ii) oversize the supercritical pumps, thus operating beyond the design point; (iii) oversize the thermal recuperator, which implies higher thermal inertia and cost. For the oxidizing mixture of the NET Power cycle, no deviations were found. Hence, all calibrated EoSs could be employed.

Future research could focus on experimentally measuring thermophysical properties of sCO_2-rich mixtures under the particular ranges of pressure, temperature and composition of the NET Power cycle working fluid. This would improve the predictive accuracy of the thermodynamic models.

CRediT authorship contribution statement

Reyes Miriam: Supervision, Funding acquisition, Conceptualization, Visualization, Writing – review & editing. **Frederiek Demeyer:** Project administration, Conceptualization, Resources, Visualization, Writing – review & editing. **Iván Velázquez:** Writing – original draft, Software, Methodology, Investigation, Formal analysis, Data curation, Conceptualization, Resources.

Declaration of Competing Interest

The authors declare that they have no known competing financial interests or personal relationships that could have appeared to influence the work reported in this paper.

Acknowledgements

This research work was funded by the University of Valladolid, Spain, through the research project 061/2209311. Authors would like to acknowledge the entities Engie and TES-H2, and the research group in thermal engines and renewable energies (MyER), from the University of Valladolid, for the technical contribution during the realization of this work.

Appendix A. Supporting information

Supplementary data associated with this article can be found in the online version at doi:10.1016/j.supflu.2025.106693.

Data Availability

Data will be made available on request.

References

[1] R. Scaccabarozzi, M. Gatti, E. Martelli, Thermodynamic analysis and numerical optimization of the NET Power oxy-combustion cycle, Appl. Energy 178 (2016) 505–526, https://doi.org/10.1016/j.apenergy.2016.06.060.
[2] W. Chan, T. Morosuk, X. Li, H. Li, Allam cycle: review of research and development, Energy Convers. Manag 294 (2023) 117607, https://doi.org/10.1016/j.enconman.2023.117607.
[3] C. Mitchell, V. Avagyan, H. Chalmers, M. Lucquiaud, An initial assessment of the value of Allam Cycle power plants with liquid oxygen storage in future GB electricity system, Int. J. Greenh. Gas. Control 87 (2019) 1–18, https://doi.org/10.1016/j.ijggc.2019.04.020.
[4] K. Wimmer, W. Sanz, Optimization and comparison of the two promising oxy-combustion cycles NET Power cycle and Graz Cycle, Int. J. Greenh. Gas. Control 99 (2020), https://doi.org/10.1016/j.ijggc.2020.103055.
[5] R.J. Allam, B.A. Forrest, J.E. Fetvedt, Method and system for power production with improved efficiency, U. S. Pat. Appl. 20180073434 (2018).
[6] L.F. González-Portillo, J. Muñoz-Antón, J.M. Martínez-Val, Thermodynamic mapping of power cycles working around the critical point, Energy Convers. Manag 192 (2019) 359–373, https://doi.org/10.1016/j.enconman.2019.04.022.
[7] I. Al-Siyabi, Effect of impurities on CO_2 stream properties, Inst. Pet. Eng. (2013).
[8] I. Tsivintzelis, G.M. Kontogeorgis, M.L. Michelsen, E.H. Stenby, Modeling phase equilibria for acid gas mixtures using the CPA equation of state. Part II: binary mixtures with CO_2, Fluid Phase Equilib. 306 (2011) 38–56, https://doi.org/10.1016/j.fluid.2011.02.006.
[9] F. Okoro, A. Chapoy, P. Ahmadi, R. Burgass, Effects of non-condensable CCUS impurities (CH_4, O_2, Ar and N_2) on the saturation properties (bubble points) of CO_2-rich binary systems at low temperatures (228.15 – 273.15 K), Greenh. Gases Sci. Technol. 14 (2024) 62–94, https://doi.org/10.1002/ghg.2252.
[10] F. Okoro, A. Chapoy, P. Ahmadi, R. Burgass, Validation of cubic EoS mixing rules and multi-fluid Helmholtz energy approximation EoS for the phase behaviour modelling of CO_2-rich binary mixtures at low temperatures, Greenh. Gases Sci. Technol. 14 (2024) 829–858, https://doi.org/10.1002/ghg.2300.
[11] G.M. Kontogeorgis, M.L. Michelsen, G.K. Folas, S. Derawi, N. Von Solms, E. H. Stenby, Ten Years with the CPA (Cubic-Plus-Association) equation of state. Part 1. Pure compounds and self-associating systems, Ind. Eng. Chem. Res. 45 (2006) 4855–4868, https://doi.org/10.1021/ie051305v.
[12] H. Li, J.P. Jakobsen, Ø. Wilhelmsen, J. Yan, PVTxy properties of CO_2 mixtures relevant for CO_2 capture, transport and storage: Review of available experimental data and theoretical models, Appl. Energy 88 (2011) 3567–3579, https://doi.org/10.1016/j.apenergy.2011.03.052.
[13] O. Kunz, W. Wagner, The GERG-2008 wide-range equation of state for natural gases and other mixtures: An expansion of GERG-2004, J. Chem. Eng. Data 57 (2012) 3032–3091, https://doi.org/10.1021/je300655b.
[14] H. Li, J. Yan, Impacts of equations of state (EOS) and impurities on the volume calculation of CO_2 mixtures in the applications of CO_2 capture and storage (CCS) processes, Appl. Energy 86 (2009) 2760–2770, https://doi.org/10.1016/j.apenergy.2009.04.013.
[15] W. Xiong, L.-H. Zhang, Y.-L. Zhao, S.-M. Wen, L.-L. Liu, Z.-L. Cao, Y.-C. Wang, S.-G. Luo, X.-Y. Jiang, Phase equilibrium modeling for CCUS fluids using a modified association equation of state, J. Supercrit. Fluids 219 (2025) 106543, https://doi.org/10.1016/j.supflu.2025.106543.
[16] M. Mazzoccoli, B. Bosio, E. Arato, Analysis and comparison of equations-of-state with p-ρ-T experimental data for CO_2 and CO_2-mixture pipeline transport, Energy Procedia 23 (2012) 274–283, https://doi.org/10.1016/j.egypro.2012.06.052.
[17] J. Gernert, R. Span, EOS-CG: a Helmholtz energy mixture model for humid gases and CCS mixtures, J. Chem. Thermodyn. 93 (2016) 274–293, https://doi.org/10.1016/j.jct.2015.05.015.

[18] T. Neumann, S. Herrig, I.H. Bell, R. Beckmüller, E.W. Lemmon, M. Thol, R. Span, EOS-CG-2021: a mixture model for the calculation of thermodynamic properties of CCS mixtures, Int. J. Thermophys. 44 (2023) 178, https://doi.org/10.1007/s10765-023-03263-6.
[19] J. Ke, N. Suleiman, Y. Sanchez-Vicente, T.S. Murphy, J. Rodriguez, A. Ramos, M. Poliakoff, M.W. George, The phase equilibrium and density studies of the ternary mixtures of CO_2 + Ar + N_2 and CO_2 + Ar + H_2, systems relevance to CCS technology, Int. J. Greenh. Gas. Control 56 (2017) 55–66, https://doi.org/10.1016/j.ijggc.2016.11.003.
[20] C. McKay, M. Nazeri, H. Haghighi, D. Erickson, Recommendations for the selection of equation of state during design and operation of impure CO2 transport and storage, 16th Int. Conf. Greenh. Gas Control Technol. GHGT-16 (2022).
[21] M. Vitali, M. Leporini, O. Masi, A. Speranza, F. Corvaro, B. Marchetti, Net zero Flow Assurance - Validation of various equations of state for the prediction of VLE and density of CO_2-rich mixtures for CCUS applications, Int. J. Greenh. Gas. Control 125 (2023) 103877, https://doi.org/10.1016/j.ijggc.2023.103877.
[22] I.E.J. Ch, R.E. Plevan, J.A. Quinn, A.I.E.J. Ch, F.H. Rhodes, C. Bridges, I.D. Robb, A. E. Alexander, H. Rosano, V.K. Lamer, T.G. Springer, R.L. Plgford, S.J.D. Van Stralen, Nether, A new two-constant equation of state, Int. J. Heat. Mass Transf. 19 (1973) 1469, https://doi.org/10.1021/i160057a011.
[23] G. Soave, Equilibrium constants from a modified Redlich-Kwong equation of state, Chem. Eng. Sci. 27 (1972) 1197–1203, https://doi.org/10.1016/0009-2509(72)80096-4.
[24] B.I. Lee, M.G. Kesler, A generalized thermodynamic correlation based on three-parameter corresponding states, AIChE 21 (1975) 510–527, https://doi.org/10.1002/aic.690210313.
[25] F. Sabozin, A. Jäger, M. Thol, Enhancement of the Lee–Kesler–Plöcker equation of state for calculating thermodynamic properties of long-chain alkanes, Int. J. Thermophys. 45 (2024) 69, https://doi.org/10.1007/s10765-024-03360-0.
[26] F.J. Ackerman, O. Redlich, On the thermodynamics of solutions. IX. Critical properties of mixtures and the equation of benedict, webb, and rubin, J. Chem. Phys. 38 (1963) 2740–2742, https://doi.org/10.1063/1.1733582.
[27] C. You, Z. Chen, X. Li, Q. Zhao, Y. Feng, C. Wang, Benedict–Webb–Rubin–Starling Equation of state + hydrate thermodynamic theories: an enhanced prediction method for CO_2 solubility and CO_2 hydrate phase equilibrium in pure water/NaCl aqueous solution system, Energies 17 (2024) 2356, https://doi.org/10.3390/en17102356.
[28] J. Gross, G. Sadowski, Perturbed-chain SAFT: an equation of state based on a perturbation theory for chain molecules, Ind. Eng. Chem. Res. 40 (2001) 1244–1260, https://doi.org/10.1021/ie0003887.
[29] J. Gross, G. Sadowski, Application of the perturbed-chain SAFT equation of state to associating systems, Ind. Eng. Chem. Res. 41 (2002) 5510–5515, https://doi.org/10.1021/ie010954d.
[30] I.K. Nikolaidis, R. Privat, J.-N. Jaubert, I.G. Economou, Assessment of the perturbed chain-statistical associating fluid theory equation of state against a benchmark database of high-quality binary-system data, Ind. Eng. Chem. Res. 60 (2021) 8935–8946, https://doi.org/10.1021/acs.iecr.1c01234.
[31] S. Arvelos, L.L. Rade, E.O. Watanabe, C.E. Hori, L.L. Romanielo, Evaluation of different contribution methods over the performance of Peng-Robinson and CPA equation of state in the correlation of VLE of triglycerides, fatty esters and glycerol + CO_2 and alcohol, Fluid Phase Equilib. 362 (2014) 136–146, https://doi.org/10.1016/j.fluid.2013.09.040.
[32] G.M. Kontogeorgis, E.C. Voutsas, I.V. Yakoumis, D.P. Tassios, An equation of state for associating fluids, Ind. Eng. Chem. Res. 35 (1996) 4310–4318, https://doi.org/10.1021/ie9600203.
[33] L. Mancuso, N. Ferrar, P. Chiesa, E. Martelli, M. Romano, Oxy-combustion turbine power plants (2025). ⟨www.ieaghg.org⟩ (accessed 12 March 2025).
[34] S.X. Hou, G.C. Maitland, J.P.M. Trusler, Measurement and modeling of the phase behavior of the (carbon dioxide + water) mixture at temperatures from 298.15 K to 448.15 K, J. Supercrit. Fluids 73 (2013) 87–96, https://doi.org/10.1016/j.supflu.2012.11.011.
[35] A. Valtz, A. Chapoy, C. Coquelet, P. Paricaud, D. Richon, Vapour-liquid equilibria in the carbon dioxide-water system, measurement and modelling from 278.2 to 318.2, K. Fluid Phase Equilib. 226 (2004) 333–344, https://doi.org/10.1016/j.fluid.2004.10.013.
[36] M.B. King, A. Mubarak, J.D. Kim, T.R. Bott, The mutual solubilities of water with supercritical and liquid carbon dioxide, J. Supercrit. Fluids 5 (1992) 296–302, https://doi.org/10.1016/0896-8446(92)90021-B.
[37] A. Bamberger, G. Sieder, G. Maurer, High-pressure (vapor + liquid) equilibrium in binary mixtures of (carbon dioxide + water or acetic acid) at temperatures from 313 to 353 K, J. Supercrit. Fluids 17 (2000), https://doi.org/10.1016/S0896-8446(99)00054-6.
[38] I. Dalmolin, E. Skovroinski, A. Biasi, M.L. Corazza, C. Dariva, J.V. Oliveira, Solubility of carbon dioxide in binary and ternary mixtures with ethanol and water, Fluid Phase Equilib. 245 (2006) 193–200, https://doi.org/10.1016/j.fluid.2006.04.017.
[39] L.L. Hnedkovský, H. Hnedkovský, R.H. Wood, V. Majer, Volumes of aqueous solutions of CH_4, CO_2, H_2S, and NH_3 at temperatures from 298.15 K to 705 K and pressures to 35 MPa, J. Chem. Thermodyn. 28 (1996) 125–142, https://doi.org/10.1006/jcht.1996.0011.
[40] H.J. Greenwood, The compressibility of gaseous mixtures of carbon dioxide and water between 0 and 500 bars pressure and 450 ° and 800 ° centigrade, Am. J. Sci. 267 (1969) 191–208, https://doi.org/10.2475/001c.125218.
[41] A. Fenghour, W.A. Wakeham, J.T.R. Watson, Densities of (water + carbon dioxide) in the temperature range 415 K to 700 K and pressures up to 35 MPa, J. Chem. Thermodyn. 28 (1996) 433–446, https://doi.org/10.1006/jcht.1996.0043.
[42] P. Chiquet, J.L. Daridon, D. Broseta, S. Thibeau, CO_2/water interfacial tensions under pressure and temperature conditions of CO_2 geological storage, Energy Convers. Manag. 48 (2007) 736–744, https://doi.org/10.1016/j.enconman.2006.09.011.
[43] M.R. Patel, P.T. Eubank, Experimental densities and derived thermodynamic properties for carbon dioxide - water mixtures, J. Chem. Eng. Data 33 (1988) 185–193, https://doi.org/10.1021/je00052a037.
[44] M.R. Patel, J.C. Holste, K.R. Hall, P.T. Eubank, Thermophysical properties of gaseous carbon dioxide-water mixtures, Fluid Phase Equilib. 36 (1987) 279–299, https://doi.org/10.1016/0378-3812(87)85029-X.
[45] L.F.S. Souza, S. Herrig, R. Span, J.P.M. Trusler, Experimental density and an improved Helmholtz-energy-explicit mixture model for (CO_2 + CO), Appl. Energy 251 (2019), https://doi.org/10.1016/j.apenergy.2019.113398.
[46] A. Cipollina, R. Anselmo, O. Scialdone, G. Filardo, A. Galia, Experimental P-T-ρ measurements of supercritical mixtures of carbon dioxide, carbon monoxide, and hydrogen and semiquantitative estimation of their solvent power using the solubility parameter concept, J. Chem. Eng. Data 52 (2007) 2291–2297, https://doi.org/10.1021/je700307r.
[47] Y. Sanchez-Vicente, T.C. Drage, M. Poliakoff, J. Ke, M.W. George, Densities of the carbon dioxide + hydrogen, a system of relevance to carbon capture and storage, Int. J. Greenh. Gas. Control 13 (2013) 78–86, https://doi.org/10.1016/j.ijggc.2012.12.002.
[48] S. Ahamada, A. Valtz, S. Chabab, L. Blanco-Martín, C. Coquelet, Experimental density data of three carbon dioxide and oxygen binary mixtures at temperatures from 276 to 416 K and at pressures up to 20 MPa, J. Chem. Eng. Data 65 (2020) 5313–5327, https://doi.org/10.1021/acs.jced.0c00484.
[49] H.B. Brugge, J.C. Holste, K.R. Hall, B.E. Gammon, K.N. Marsh, Densities of Carbon Dioxide + Nitrogen from 225 K to 450 K at Pressures up to 70 MPa (1997), https://doi.org/10.1021/je970044w.
[50] H.A. Duarte-Garza, J.C. Holste, K.R. Hall, K.N. Marsh, B.E. Gammon, Isochoric pVT and phase equilibrium measurements for carbon dioxide + nitrogen, J. Chem. Eng. Data 40 (1995) 704–711, https://doi.org/10.1021/je00019a038.
[51] M.E. Mondéjar, M.C. Martín, R. Span, C.R. Chamorro, New (p, ρ, T) data for carbon dioxide - Nitrogen mixtures from (250 to 400) K at pressures up to 20 MPa, J. Chem. Thermodyn. 43 (2011) 1950–1953, https://doi.org/10.1016/j.jct.2011.07.006.
[52] J.C. Seitz, J.G. Blencoe, Volumetric properties for {(1-x)CO_2 + xCH_4}, {(1-x)CO_2 + xN_2}, and {(1-x)CH_4 + xN_2} at the pressures (19.94, 29.94, 39.94, 59.93, 79.93, and 99.93) MPa and the temperature 673.15 K, J. Chem. Thermodyn. (1996) 1207–1213, https://doi.org/10.1006/jcht.1996.0107.
[53] J.F. Ely, W.M. Haynes, B.C. Bain, Isochoric (p, V_m, T) measurements on CO_2 and on (0.982CO_2 + 0.018N_2) from 250 to 330 K at pressures to 35 MPa, J. Chem. Thermodyn. (1989) 879–894, https://doi.org/10.1016/0021-9614(89)90036-0.
[54] C. Zhao, J. Lv, G. Li, Q. Zhang, Y. Zhang, S. Liu, Y. Chi, Densities of CO_2/N_2/O_2 ternary mixtures at temperatures from (300.15 to 353.15) K and pressures from (5 to 18) MPa, Thermoch. Acta 676 (2019) 20–26, https://doi.org/10.1016/j.tca.2019.03.032.
[55] M. Mantovani, P. Chiesa, G. Valenti, M. Gatti, S. Consonni, Supercritical pressure-density-temperature measurements on CO_2-N_2, CO_2-O_2 and CO_2-Ar binary mixtures, J. Supercrit. Fluids 61 (2012) 34–43, https://doi.org/10.1016/j.supflu.2011.09.001.
[56] C. Rivas, S.T. Blanco, J. Fernández, M. Artal, I. Velasco, Influence of methane and carbon monoxide in the volumetric behaviour of the anthropogenic CO_2. Experimental data and modelling in the critical region, Int. J. Greenh. Gas. Control 18 (2013) 264–276, https://doi.org/10.1016/j.ijggc.2013.07.019.
[57] S. Liu, C. Zhao, J. Lv, P. Lv, Y. Zhang, Density Characteristics of the CO_2-CH_4 binary system: experimental data at 313–353 K and 3–18 MPa and modeling from the PC-SAFT EoS, J. Chem. Eng. Data 63 (2018) 4368–4380, https://doi.org/10.1021/acs.jced.8b00433.
[58] Aspen Plus | Leading Process Simulation Software | AspenTech, (n.d.). ⟨https://www.aspentech.com/en/products/engineering/aspen-plus⟩ (accessed June 12, 2023).
[59] The MathWorks Inc, MATLAB version: 9.13.0 (R2022b), (2022). ⟨https://www.mathworks.com⟩ (accessed June 12, 2023).
[60] H. Wu, B. Zhang, W. Wang, H. Jin, Optimizing phase equilibrium predictions for the liquefaction of supercritical water gasification products: enhancing energy storage solutions through advanced thermodynamic modeling, Energy 308 (2024) 132845, https://doi.org/10.1016/j.energy.2024.132845.
[61] E. Cruz Sánchez-Alarcos, M.T. Garcia, I. Gracia, J.F. Rodriguez, J.M. Garcia-Vargas, Modelling of the equilibrium of supercritical CO_2 + lavender essential oil with Aspen Plus®, J. Supercrit. Fluids 209 (2024) 106239 https://doi.org/10.1016/j.supflu.2024.106239.
[62] H.I. Britt, R.H. Luecke, The estimation of parameters in nonlinear, implicit models, Technometrics 15 (1973) 233, https://doi.org/10.2307/1266984.

[63] Cengel Yunus A., Boles Michael A., Thermodynamics. An Engineering Approach., 7th ed., Nevada, 2011.
[64] H. Li, B. Dong, Z. Yu, J. Yan, K. Zhu, Thermo-physical properties of CO_2 mixtures and their impacts on CO_2 capture, transport and storage: progress since 2011, Appl. Energy 255 (2019), https://doi.org/10.1016/j.apenergy.2019.113789.
[65] M. Carolina, D. Ramos, F.J. Blas, A. Galindo, Modelling the phase equilibria and excess properties of the water + carbon dioxide binary mixture, Fluid Phase Equilib. 261 (2007) 359–365, https://doi.org/10.1016/j.fluid.2007.07.012.
[66] M. Ibrahim, G. Skaugen, I.S. Ertesvåg, T. Haug-Warberg, Modelling CO_2 - water mixture thermodynamics using various equations of state (EoSs) with emphasis on the potential of the SPUNG EoS, Chem. Eng. Sci. 113 (2014) 22–34, https://doi.org/10.1016/j.ces.2014.03.025.
[67] R.M. Cuéllar-Franca, A. Azapagic, Carbon capture, storage and utilization technologies: a critical analysis and comparison of their life cycle environmental impacts, J. CO_2 Util. 9 (2015) 82–102, https://doi.org/10.1016/j.jcou.2014.12.001.